IMPACT OF INHOMOGENEOUS UNSTEADY PARTICIPATING MEDIA IN A COUPLED CONVECTION–RADIATION SYSTEM USING FINITE ELEMENT BASED METHODS

J. E. Avalos-Patiño, S. Dargaville, S. J. Neethling, M. D. Piggott

Department of Earth Science & Engineering, Imperial College London, UK

Abstract

Combined convection–radiation is a common phenomenon in many engineering problems. A differentially–heated rectangular enclosure is a widely–used benchmark for testing numerical techniques developed for solving the coupled momentum and energy equations related to combined convection–radiation. Previous studies have tended to describe the phenomenon in cases using simplified characteristics for the participating media including the assumptions of: (*i*) uniform distribution, (*ii*) homogeneous cross section, (*iii*) grey gas radiation and (*iv*) under steady state conditions. The effects of an inhomogeneous unsteady participating media, e.g. composed of a mixture of gases, are arguably understudied. In this work the effect of an inhomogeneous unsteady participating media on combined convection–radiation inside a rectangular enclosure is considered, under both grey and non-grey gas modelling approaches involving a mixture of gases. A key novelty in this work is the inclusion of the ability to handle inhomogeneous participating media which change in space, time and absorption cross section values as a result of the convection–radiation coupling, allowing us to assess different gas modelling approaches. A global gas radiation model is used and a new non–uniform discretisation method for the absorption distribution function is introduced; this method allows a better handling of those energy groups in which the Planck absorption coefficient is low, improving the performance of the spherical harmonics method and mitigating ray–effects on finite elements in angle discretisation. The momentum and energy equations are solved numerically using finite element based discretisation methods. The radiative transfer equation is solved numerically using both spherical harmonics and finite elements for the angular discretisation, with their relative performance compared. The results highlight the importance that the characteristics of the participating media can have on the convection phenomenon and therefore on the resulting temperature field.

Keywords: Coupled convection–radiation, inhomogeneous unsteady participating media, gas radiation model, finite elements method.

Nomenclature

a	Absorption distribution function weight values (−)
B_r	Ratio of Boltzmann populations (−)
C	Absorption cross section ($\mathrm{cm^2\ molecule^{-1}}$)
c_2	Second radiation constant (1.438777 cm K)
E''	Lower–state energy ($\mathrm{cm^{-1}}$)
E_r	Ratio of stimulated emissions (−)
E_b	Planck's function
$\mathscr{F}$	Absorption distribution function
f_L	Spectral lines shape function
G	Incident radiation ($\mathrm{W\ m^{-2}}$)
$\mathscr{G}$	Angular basis functions
I	Radiative intensity ($\mathrm{W\ m^{-2}}$)
I_b	Blackbody intensity ($\mathrm{W\ m^{-2}}$)
N	Molar density ($\mathrm{mol\ m^{-3}}$)
$\hat{\mathbf{n}}$	Outward normal vector
p	Pressure (Pa)
Q_r	Ratio of total internal partition sum values (−)
$\mathbf{q_r}$	Radiative heat flux ($\mathrm{W\ m^{-2}}$)
$\mathbf{r}$	Spatial position
S	Spectral line intensity at $T = 296$ K ($\mathrm{cm^{-1}\ (molecule^{-1}\ cm^2)}$)
S^*	Spectral line intensity at $T \neq 296$ K ($\mathrm{cm^{-1}\ (molecule^{-1}\ cm^2)}$)
T	Temperature (K)
t	Time (s)
$\mathbf{u}$	Velocity ($\mathrm{m\ s^{-1}}$)
w	Basis functions for finite elements discretisation
X	Molar fraction (−)
Y	Real orthonormal spherical harmonics

Greek symbols

δ	Pressure shift of spectral lines position ($\mathrm{cm^{-1}\ atm}$)
ϵ_w	Boundary emissivity (−)
γ	Spectral line pressure–broadened half width at half maximum ($\mathrm{cm^{-1}\ atm}$)
κ_ν	Absorption coefficient ($\mathrm{cm^{-1}}$)
κ_p	Plank absorption coefficient ($\mathrm{cm^{-1}}$)
ν	Spectral line position ($\mathrm{cm^{-1}}$)
ν^*	Shifted spectral line position ($\mathrm{cm^{-1}}$)
$\overline{\overline{\alpha}}$	Thermal diffusivity ($\mathrm{m^2\ s^{-1}}$)
$\overline{\overline{\nu}}$	Kinematic viscosity ($\mathrm{m^2\ s^{-1}}$)
ϕ	Scalar tracer (−)
ρ	Density ($\mathrm{kg\ m^{-1}}$)
ρ''	Boundary reflectance (−)
σ	Stefan–Boltzmann constant (5.67×10^{-8} $\mathrm{W\ m^2\ K^4}$)
$\mathbf{\Omega}$	Angular direction (rad)

1. Introduction

Combined convection–radiation is a common phenomenon in many engineering problems including electronic devices cooling, furnaces and building ventilation [1, 2, 3, 4]. A typical combined convection–radiation scenario is the case of natural convection inside a rectangular enclosure with differentially–heated walls [5]. This test case has been widely used both experimentally and numerically to describe the coupling of radiation and flow fields. Miroshnichenko & Sheremet [6] present an exhaustive review of experimental and numerical methods applied to natural convection in rectangular enclosures, including some studies that

assess the effects of radiation. Experimental studies have faced some challenges related to their accuracy, mainly due to the high sensitivity of the fluid flow inside the cavity to the experimental conditions [6, 7, 8]. In many of the experimental studies a tandem numerical simulation has been carried out in order to evaluate the agreement between experimental and numerical results. For example, Tian & Karayiannis [7] and Ampofo & Karayiannis [8] considered experimental studies and demonstrated high accuracy for the obtained numerical results. These works have thus been used as a benchmark for numerical models.

In rectangular enclosures, radiation effects can be related to both walls and gas radiation [9]. In both cases the radiative intensity depends on material properties. In the case of walls, radiation is characterised by the emissivity value, whilst in the case of gas radiation it is characterised by the molecular cross section of the participating media [10]. Gas radiation properties depend strongly on the absorption spectrum of the participating media. Computing this involves integrating the radiative transfer equation over the spectrum, making this process complex and expensive [11]. A way to simplify this issue is to assume that the participating medium is a so–called grey gas; this implies that the radiative properties of the gas are reduced to a single mean value. However, it should be noted that this approximation is not advisable for evaluating the effect of thermal radiation due to its reduced accuracy. Contrary to the grey gas approximation, the line–by–line method involves solving the radiative transfer equation for every spectral line, making the method the most accurate but also the most expensive considering that millions of spectral lines can be found in a particular spectral resolution [11].

In order to find a practical and feasible way to solve the radiative transfer equation considering the spectral dependence of the gas cross section, different non-grey radiation models have been developed. These methods can be classified into two categories: narrow band models and global or full spectrum models [12]. In narrow band models, the spectrum is divided into small spectral intervals containing hundreds of lines, in which the radiative properties of the gas are averaged. The accuracy of these models is close to that obtained with line–by–line calculations; however, these methods are still expensive compared to global models [11, 12].

Global models allow the integration of radiative transfer for the full spectrum of the participating gas while demanding less computational resource and achieving good accuracy [13, 14]. However, global models have some limitations, such as the need for grey boundaries [15].

In realistic problems, such as combustion systems, the participating gases are composed of multiple species. Different approaches to approximate the effect of the mixture of gases on radiation have been described in previous studies. In some studies the radiative transfer

equation has been solved for mixtures of gases using line–by–line methods; however, in the majority of cases high computational cost has been remarked upon [16, 17]. Other studies compare the performance of narrow band models and global models. Chu et al. [18] compared narrow band and global models for a mixture of gases under different pressures, concluding that in global methods the accuracy is decreased at high pressures and in some cases near the boundaries, while narrow band models are accurate in all cases, but computationally expensive. Goutiere et al. [13] and Pierrot et al. [15] compared a set of narrow band and global models in enclosures containing mixtures of CO_2–H_2O. Both studies highlight the accuracy of narrow band models; however, global models based on an absorption–line blackbody distribution function yield good accuracy being significantly less expensive than narrow band models. Solovjov & Webb [19] tested different approaches to deal with a mixture of gases and compared three methods to calculate the corresponding distribution function required for global models. In the first method it is assumed that the spectral lines of each gas do not significantly overlap, therefore a single discretisation of the cross section is required, simplifying the calculations. The second method considers the probability of intersection of each gas spectrum, assuming that the gas cross sections are uncorrelated, hence the calculation of the distribution function can be reduced to a multiplication. Finally, the third method combines both previous considerations, applying the first for the higher values of the cross section where overlapping is less probable and the second for the lower values where the probability of intersection is high. This study concludes that the proposed methods do not affect accuracy significantly while retaining low computational cost by reducing the need to calculate multiple integrals to only one. Despite the participating media in these studies being considered inhomogeneous, the mixture of gases is considered to be at steady state.

The development and usage of numerical methods for solving the radiative transfer equation is of significant importance for natural convection problems. This is because radiation can have a strong effect on natural convection due to the dependency of the flow fields on temperature [20]. This coupled effect was studied in detail by Soucasse et al. [21] finding that wall and gas radiation lead to flow circulation in rectangular enclusores, and this flow circulation is stronger in combined wall–gas radiation problems.

Two common deterministic methods for the discretisation of the radiative transfer equation are the spherical harmonics method (via a so-called P_N expansion) and the discrete ordinates method (DOM or via a so-called S_N expansion). The spherical harmonics method is an approach to solve the radiative transfer equation by expressing the angular dependency of the radiative intensity at a point via a series of spherical harmonics. The number of equations

is related to the term at which the series is truncated, specifically the relation is $(N+1)^2$. This value gives the method its order and name [10]. However, this implies a disadvantage in terms of computational cost if the series is truncated at higher values of N. One advantage of the method is the fact that solutions are free of ray effects, however unphysical oscillations can be observed in regions with anisotropy in the angular flux [22], which can result in slower convergence in optically thin participating media. This can be a serious disadvantage when using a global gas radiation method, considering that some energy groups, defined by the discrete cross section values, could have low Planck absorption coefficients.

Sun, Zhang and Howell [23, 5] assessed the performance of P_1, P_3 and SP_3 (simplified P_3) methods for combined convection–radiation inside a rectangular enclosure. For this test all the walls were considered as black boundaries and the participating medium as absorbing, emitting and non–scattering. The method was validated by comparing the results with those obtained using the Monte–Carlo Method, which is known to be accurate but computationally expensive. These methods showed poor accuracy for optically thin participating media, with better accuracy for optically thick cases. Additionally, in the case of the P_3 and SP_3 methods the computational costs is also increased.

The discrete ordinates method (S_N) is one of the most extensively used approaches for radiative transfer modelling, offering good accuracy, reasonable computational cost and compatibility with the models used for other transfer phenomena [24]. This method is particularly popular due to its simplicity considering that the angular dependency in the solutions is limited to a discrete set of directions; however, this leads to its major disadvantage – ray effects [22]. Ray–effects, much like the unphysical oscillations in spherical harmonics, manifest when the discrete cross section is low. Modelling radiative transfer in optically thin media is therefore challenging regardless of the choice of angular discretisation.

Another method for solving the radiative transfer equation is the finite element method. This method has been used in combined convection–radiation problems [25] and imaging applications for medical devices [26]. In the finite element method, the angular dependence of the radiative intensity is limited to a function space spanned by a set of basis functions [27]. The application of the finite element method can be advantageous due to the possibility of implementing sophisticated discretisations that provide improvements to accuracy and computational performance [28, 27]. We should note however that any angular discretisation that is not rotationally invariant will suffer from ray–effects, e.g., a P_0 finite element method in angle will show ray–effects like that of a similar discrete ordinates method [29]; the two approaches however are not exactly equivalent [30].

Most of the previous studies related to the combined convection–radiation problem consider either uniform distribution, homogeneous cross section, grey gas radiation or steady state as a condition for the participating media, therefore the analysis of the combined convection–radiation problem with varying properties remains a challenge. Additionally, in those cases that consider non–grey gas radiation using global models, the effect of the spectral resolution and number of discrete cross sections has not been assessed.

The purpose of this work is to analyse the effect of an inhomogeneous unsteady participating media in the combined convection–radiation problem in a differentially–heated rectangular cavity, including the assessment of non–grey radiation under a global gas model approach. We use both finite element discretisation and a spherical harmonics based method in angle, in order to compare the performance of these different approaches. Importantly we introduce a new non–uniform discretisation of the absorption distribution function, which ensures that all discrete cross section values lead to the Planck absorption coefficients greater than the optically thin limit. This is designed to improve the performance of the spherical harmonics method without significantly compromising accuracy. This comparison is of particular interest for problems where the characteristics of the participating media change in space, time and cross section absorption values, therefore comparing both methods illustrates the sensitivity of each method to these conditions, and our new discretisation of the absorption distribution function. The effect of gas radiation on convection observed in this work is consistent with the findings by Soucasse et al. [21]. While that work used the inherently expensive ray tracing approach to solve the RTE, here we consider the more efficient approaches of finite elements in angle and spherical harmonics. Therefore, the present work offers a computationally cheaper alternative for simulating the effect of wall and gas radiation in coupled convection–radiation problems, without the need to use ray tracing which is impractical for large scale problems.

2. Governing equations

2.1. Natural convection problem

Natural convection is described here by the incompressible Navier–Stokes and Energy equations under the Boussinesq approximation:

$$\frac{\partial \mathbf{u}}{\partial t} + \mathbf{u}\cdot\nabla\mathbf{u} + \nabla p' - \nabla\cdot(\overline{\overline{\nu}}\nabla\mathbf{u}) = \rho'\boldsymbol{g}, \tag{1}$$

$$\nabla\cdot\mathbf{u} = 0, \tag{2}$$

$$\frac{\partial T}{\partial t} + \mathbf{u}\cdot\nabla T - \nabla\cdot(\overline{\overline{\alpha}}\nabla T) = -\nabla\cdot\mathbf{q_r}, \tag{3}$$

$$\frac{\partial \phi}{\partial t} + \mathbf{u}\cdot\nabla\phi - \nabla\cdot(\overline{\overline{D}}\nabla\phi) = 0, \tag{4}$$

where $\mathbf{u}$ is the velocity vector, p' is the perturbation pressure, $\overline{\overline{\nu}}$ is the kinematic viscosity, $\rho' = \Delta\rho/\rho_0$ is the perturbation density, T is the temperature, $\overline{\overline{\alpha}}$ is the thermal diffusivity, $\mathbf{q_r}$ is the radiative heat flux vector, ϕ is a scalar tracer that represents the concentration of species within the domain and $\overline{\overline{D}}$ is the diffusivity tensor associated with this field.

The divergence of the radiative heat flux at wavenumber ν is given by [10]:

$$\nabla\cdot\mathbf{q_r} = \kappa_\nu(4\pi I_{b_\nu} - G_\nu), \tag{5}$$

where κ_ν is the absorption coefficient, I_{b_ν} is the blackbody intensity and G_ν is the incident radiation, which has to be calculated by solving the Radiative Transfer Equation (RTE).

2.2. Radiative Transfer Equation – RTE

The RTE for an absorbing, emitting, non–scattering medium at wavenumber ν is [10]:

$$\boldsymbol{\Omega}\cdot\nabla I_\nu(\mathbf{r},\boldsymbol{\Omega}) = \kappa_\nu(\mathbf{r})(I_{b_\nu}(\mathbf{r}) - I_\nu(\mathbf{r},\boldsymbol{\Omega})), \tag{6}$$

where $I_\nu(\mathbf{r},\boldsymbol{\Omega})$ is the radiative intensity at point $\mathbf{r}$ and direction $\boldsymbol{\Omega}$, $I_{b_\nu}(\mathbf{r})$ is the blackbody intensity at point $\mathbf{r}$, $\kappa_\nu(\mathbf{r})$ is the absorption coefficient at point $\mathbf{r}$.

Appropriate boundary conditions for Eq. (6) may be written in the form:

$$I(\mathbf{r_w},\hat{\mathbf{s}}) = \epsilon_w(\mathbf{r_w})I_b(\mathbf{r_w}) + \int_{\hat{\mathbf{n}}\cdot\hat{\mathbf{s}}'<0} \rho'' I(\mathbf{r_w},\hat{\mathbf{s}}')|\hat{\mathbf{n}}\cdot\hat{\mathbf{s}}'|d\hat{\mathbf{s}}', \tag{7}$$

where $\hat{\mathbf{n}}$ is the outward surface normal, ϵ_w is the emissivity of the boundary and ρ'' is the reflectance of the boundary and varies according to the type of reflection (diffuse or specular).

The radiative power is the quantity that is involved in (3) and is defined as the difference between the absorbed and the emitted radiative power. The radiative power takes the form

of the opposite of the divergence of the radiative flux $\mathbf{q_r}$ as shown in Eq. (6), with $G_\nu = \int_{\mathbf{\Omega}} I_\nu(\mathbf{r}, \mathbf{\Omega}) d\mathbf{\Omega}$.

3. Numerical methods

The following numerical methods were applied for the solution of this problem.

3.1. Fluid flow

The natural convection equations (1) were numerically solved using the Finite Element Method with no–slip boundary condition ($\mathbf{u} \cdot \hat{\mathbf{n}} = 0$) at the walls which yields the semi–discrete system

$$M\dot{\mathbf{u}} + A\mathbf{u} + Cp - K\mathbf{u} = b, \tag{8}$$

where the finite element discrete matrices are given by:

$$M = \int_\Omega w_i \cdot w_j, \quad A = \int_\Omega w_i(\mathbf{u} \cdot \nabla w_j), \quad C = \int_\Omega w_i \cdot \nabla w_j, \quad K = \int_\Omega \nabla w_i \cdot \nabla w_j, \quad b = \int_\Omega w_i \cdot \rho' \boldsymbol{g},$$

with w_i and w_j basis functions which belong to an appropriate function space, and where the volume differentials in these integrals have been dropped for brevity.

For the temporal discretisation, here $\dot{\mathbf{u}}$ is approximated using Crank–Nicolson time stepping (implemented via a Θ scheme with the choice $\Theta = 1/2$). This yields the fully discrete system

$$M\left(\frac{\mathbf{u}^n - \mathbf{u}^{n-1}}{\Delta t}\right) = \Theta(b - A\mathbf{u}^n - Cp + K\mathbf{u}^n) + (1-\Theta)(b - A\mathbf{u}^{n-1} - Cp + K\mathbf{u}^{n-1}). \tag{9}$$

3.2. Radiative transfer

For the spatial discretisation of the RTE in space a Sub–Grid Scale model (SGS) is used. This model decomposes the solution into two components approximated by a finite element formulation – a coarse component and a sub–grid component. The sub–grid component handles instability and oscillations related to a continuous finite element discretisation [31, 32, 33, 34, 25].

For the angular discretisation of the RTE, the intensity is represented by the span of $\mathscr{M}$ angular basis functions:

$$I(\mathbf{r}, \mathbf{\Omega}) \simeq \sum_{q=1}^{\mathscr{M}} I_q(\mathbf{r}) \mathscr{G}_q(\mathbf{\Omega}), \tag{10}$$

where $\mathscr{G}_q(\mathbf{\Omega})$ are the angular basis functions and $I_q(\mathbf{r})$ are the coefficients of the projection onto the basis.

In this work, the spherical harmonics method and a finite element method in angle, with P_0 (constant) basis functions on each element, were applied.

3.2.1. Spherical Harmonics (P_N)

In the spherical harmonics method the RTE is expressed in terms of a spherical harmonics expansion up to order N:

$$I(\mathbf{r},\mathbf{\Omega}) \simeq \sum_{l=0}^{N} \sum_{m=-l}^{l} I_l^m(\mathbf{r}) Y_l^m(\mathbf{\Omega}), \tag{11}$$

where $Y_l^m(\mathbf{\Omega})$ are the real orthonormal spherical harmonics.

3.2.2. Finite Elements

The finite element formulation consists of dividing the angular domain into $\mathscr{M} = N \times (N+2)$ nonoverlapping angles $\Delta\Omega_q$. In this case P_0 (constant) basis functions are defined on each element over each angle as in [27]:

$$\mathscr{G}_q(\mathbf{\Omega}) = \begin{cases} 1 & \text{if } \mathbf{\Omega} \in \Delta\Omega_q, \\ 0 & \text{otherwise.} \end{cases} \tag{12}$$

4. Gas radiation model

The spectral intensity at wavenumber ν can be calculated using (6). However, in order to calculate the total intensity it is necessary to integrate the RTE over the spectrum. This can by performed using a Line–by–Line (LBL) or a Global Model. LBL models are discrete approximations of the continuous spectrum, such that the RTE is solved for each discrete spectral intensity and then integrated over all wavenumbers. LBL models require solutions at several wavenumbers in order to represent a spectral range, which makes this model accurate but highly expensive. In contrast, in global models the total intensity is calculated by integrating the RTE over fractions of intensity which are summed to calculate the total intensity [12].

In this study, a Global Model based on an absorption distribution function (ADF) as described in [14] is used. The absorption distribution function ($\mathscr{F}$) describes the fraction of blackbody emissive power that lies in the spectrum cross section region below a maximum cross section value C:

$$\mathscr{F}(C) = \frac{1}{\sigma T^4} \int_{\{\nu: C_\nu < C\}} E_{b\nu}\, d\nu, \tag{13}$$

where σT^4 is the total blackbody radiation power with σ the Stefan–Boltzmann constant and T the gas temperature. E_b is Planck's function.

The absorption distribution function is a cumulative distribution function which allows for the discretisation the cross section as C_i values within intervals $[C_i^-, C_i^+]$ with corresponding weight values calculated as:

$$a_i = \mathscr{F}(C_i^+) - \mathscr{F}(C_i^-). \tag{14}$$

This discretisation of the absorption distribution function allows to write Eq. (6) as:

$$\mathbf{\Omega} \cdot \nabla I_i(\mathbf{r}, \mathbf{\Omega}) = \kappa_i(\mathbf{r})(a_i I_b(\mathbf{r}) - I_i(\mathbf{r}, \mathbf{\Omega})), \tag{15}$$

where κ_i is the discrete absorption coefficient.

The total intensity is the result of the contribution of each fraction of intensity calculated using Eq. (15) as:

$$I = \sum_i I_i. \tag{16}$$

In this work data from the HITRAN2016 database [35] has been used for calculating the line–by–line absorption cross section. These data requires an initial treatment in order to define the profile function that describes the cross section. This has been performed using the Lorentz broadening function for the lines shape:

$$f_L = \frac{1}{\pi}\left(\frac{\gamma}{\gamma^2 + (\nu - \nu^*)^2}\right), \tag{17}$$

where γ is the line pressure–broadened half width at half maximum, ν is the line position and ν^* is the shifted line position due to pressure. γ and ν^* are calculated using the following equations:

$$\nu^* = \nu + \delta p_{\text{ref}}, \tag{18}$$

$$\gamma = \left(\frac{T_{\text{ref}}}{T}\right)^{n_{\text{air}}} (\gamma_{\text{air}}(p_{\text{ref}} - p_{\text{self}}) + \gamma_{\text{self}} p_{\text{self}})), \tag{19}$$

where δ is the pressure shift of the line position at reference pressure, p is the gas pressure, $T_{\text{ref}} = 296$ K and $p_{\text{ref}} = 1$ atm are reference temperature and pressure, n_{air} is the temperature dependence coefficient and p_{self} is the partial pressure of the gas. The line intensity at a temperature different than $T_{\text{ref}} = 296$ K is calculated as:

$$S^* = S \cdot Q_r \cdot B_r \cdot E_r, \tag{20}$$

where S is the line intensity at $T_{\text{ref}} = 296$ K found in HITRAN database [35], Q_r is the ratio of total internal partition sum values, B_r is the ratio of Boltzmann populations and E_r is the

ratio of stimulated emissions. These ratios are defined as:

$$Q_r = \frac{Q_{T_{\text{ref}}}}{Q_T}, \tag{21}$$

$$B_r = \frac{\exp(-c_2 \cdot {}^{E''}/_{T})}{\exp(-c_2 \cdot {}^{E''}/_{T_{\text{ref}}})}, \tag{22}$$

$$E_r = \frac{1 - \exp(-c_2 \cdot {}^{\nu}/_{T})}{1 - \exp(-c_2 \cdot {}^{\nu}/_{T})}, \tag{23}$$

where $Q_{T_{\text{ref}}}$ and Q_T are the total internal partition sum values at reference temperature ($T_{\text{ref}} = 296$ K) and gas temperature respectively, $c_2 = 1.438777$ cm^{-1}K is the second radiation constant and E'' is the lower–state energy of the transition. E'' values are included in the line–by–line parameters in HITRAN database [35] and Q values are calculated using the code TIPS [36].

The absorption cross section is defined as:

$$C = S^* \cdot f_L. \tag{24}$$

The global gas radiation model has been computed following the procedure described in [12]. The cross section of each gas was discretised into n intervals $[C_i^-, C_i^+]$, $i = 1, 2, ..., n$, using a logarithmic scale:

$$C_i^- = C_{\min}\left(\frac{C_{\max}}{C_{\min}}\right)^{(i-1)/n}, \tag{25}$$

$$C_i^+ = C_{\min}\left(\frac{C_{\max}}{C_{\min}}\right)^{i/n}. \tag{26}$$

The mean value of the interval C_i and the corresponding wavenumber Δ_i are defined as:

$$C_i = \left(C_i^- \cdot C_i^+\right)^{1/2}, \tag{27}$$

$$\Delta_i = \{\nu \mid C_i^- < C_i < C_i^+\}. \tag{28}$$

The discrete form of the absorption distribution function, Eq. (13), is:

$$\mathscr{F}(C) = \frac{1}{\sigma T^4} \sum_{j=1}^{n} \left(\int_{\Delta_j} E_{b_\nu} \, d\nu \right)_j. \tag{29}$$

The weights for each discrete cross section C_i are calculated using Eq. (14), and the discrete absorption coefficients are calculated each discrete cross section value as:

$$\kappa_i = NXC_i, \tag{30}$$

with N and X being the molar density and the molar fraction of the participating gas. For an ideal gas $N = p/kT$ where k is the Boltzmann constant.

This procedure is summarised in the following algorithm:

Algorithm 1: Global gas radiation model

Result: Absorption coefficients and weights

Read data from HITRAN database

Calculate line profile (Eq. (17))

Calculate line intensity (Eq. (20))

Calculate cross section (Eq. (24))

Discretise cross section into n intervals (Eq. (25))

for i = *1,...,n* **do**

  Calculate interval cross section mean value C_i (Eq. (27))

  Calculate spectral interval Δ_i (Eq. (28))

  for j = *1,...,i* **do**

    Calculate the cumulative distribution function $\mathscr{F}(C_i)$ (Eq. (13))

  end

  Calculate absorption coefficients weights (Eq. (14))

  Calculate absorption coefficients (Eq. (30))

end

4.1. Test of the methods

One of the cases studied in [13] was selected to test the numerical methods and the gas radiation model presented in this work. The selected test consists of a rectangular enclosure in which energy transfer is dominated by radiation, emulating a steady-state flame, with constant molar fractions of H_2O (20%) and CO_2 (10%), and a temperature field defined as in Eq. (31) and shown in figure 1.

$$T(x,y) = \begin{cases} (14000x - 400)(1 - 3y_0^2 + 2y_0^3) + 800 & \text{if } x \leq 0.1, \\ -\frac{10000}{9}(x-1)(1 - 3y_0^2 + 2y_0^3) + 800 & \text{if } x > 0.1, \end{cases} \tag{31}$$

$$y_0 = \frac{|0.25 - y|}{0.25}. \tag{32}$$

The spatial domain was discretised in an unstructured mesh with 5396 triangular elements. The RTE was solved using both spherical harmonics (P_3) and finite element expansions (6 discrete angles) for each of the global gas radiation model discretisation cases mentioned before. The numerical solution of the problem was achieved using the code FETCH2 [37, 38, 39] which is composed of solvers for the RTE coupled to the CFD code Fluidity [40, 41]. Additional code

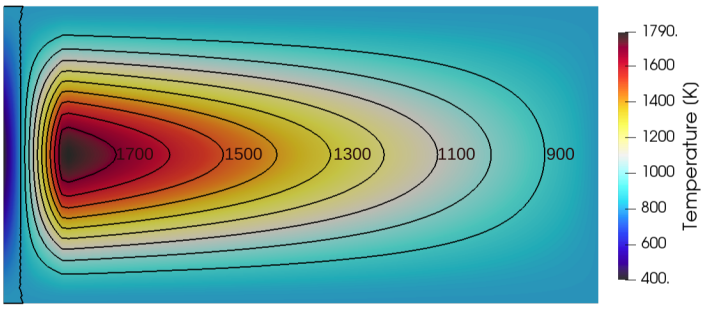

Figure 1: Temperature field for the simulated steady-state flame defined by Eq. (31). Isothermal lines in black.

was developed for calculating the absorption cross section profile function and for the global gas radiation model from HITRAN data. All the simulations have been run in an 8–core Intel® Xeon® E5–2630 v3 CPU at 2.40 GHz with 64 GB RAM, running Ubuntu 16.04 LTS.

Considering the presence of different species in the participating media, it is necessary to define the absorption cross section of the mixture. Different approaches for modelling the properties of the mixture are presented in [19]. The selection of the approach is related to the correlation and the overlapping between the cross sections of the different gases.

Figure 2 shows the absorption cross section profile function of each species. These cross sections only overlap at very low values. This allows the use of a superposition approach to define the absorption cross section of the mixture. Under this approach, the mixture of gases can be treated as a single gas, thus only one cross section discretisation is required. For this single gas, which represents the mixture, the absorption cross section, the absorption coefficient and the absorption distribution function are defined as shown in Eq. (33). The absorption coefficient function of the mixture at three different spectral resolutions is shown in figure 3.

$$C_\nu = X_{H_2O} C_{H_2O\nu} + X_{CO_2} C_{CO_2\nu}, \tag{33}$$

$$\mathscr{F}(C_\nu) = \mathscr{F}_{X_{H_2O} C_{H_2O}}(C) + \mathscr{F}_{X_{CO_2} C_{CO_2}}(C) - 1, \tag{34}$$

$$\kappa_i = N C_\nu. \tag{35}$$

In order to assess the performance of the global gas radiation model, the absorption cross section profile function has been generated at the spectral range 0–3000 cm^{-1} with three different resolutions: 5, 0.5 and 0.05 cm^{-1}, and absorption distribution function has been calculated using different numbers of discrete cross sections. This enables the assessment of the sensitivity and the effect on the computational cost of the resolution of the absorption cross section profile function and the discretisation of the cross section.

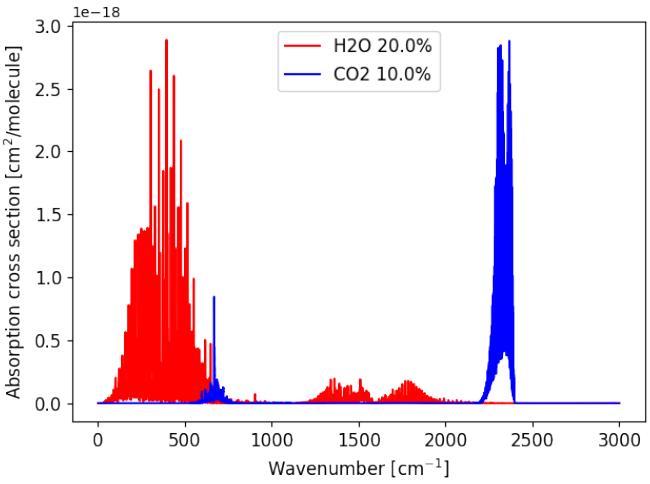

Figure 2: Absorption cross sections of participating gases.

The discretisation of the cross section in the global gas radiation model is also relevant for the performance of the solver used for the RTE, considering that the radiative intensity is calculated for each discrete absorption cross section value defined in the global gas radiation model.

The absorption coefficient function of the mixture at the three different spectral resolutions is shown in figure 3. A particular cross section discretisation case (10 discrete cross sections) has been included in this figure in order to show that most of the discrete cross section values are very small, which is characteristic of an optically thin participating media. Figure 4a shows the absorption distribution functions for the three cases displayed in figure 3. Additionally, figure 4b shows the absorption distribution functions at different numbers of discrete cross sections for the maximum spectral resolution case (0.05 cm^{-1})

The computation time for the gas radiation model is shown in figure 4c. Both absorption cross section profile function resolution and cross section discretisation have a significant effect on the computation time of the gas radiation model. However, the effect of absorption cross section profile function resolution is significantly higher.

The results are compared with the results presented in [13] and other studies that used this test case for assessing RTE solvers. A summary of the methods applied in these studies is presented in table 1.

The radiative power along the midline $y = 0.25$ was calculated and compared with the results of the studies cited in table 1. Results are displayed in figure 5. The accuracy of the methods was measured by comparing the radiative power along the midline $y = 0.25$ using spherical harmonics and finite element expansions with respect to the selected benchmark.

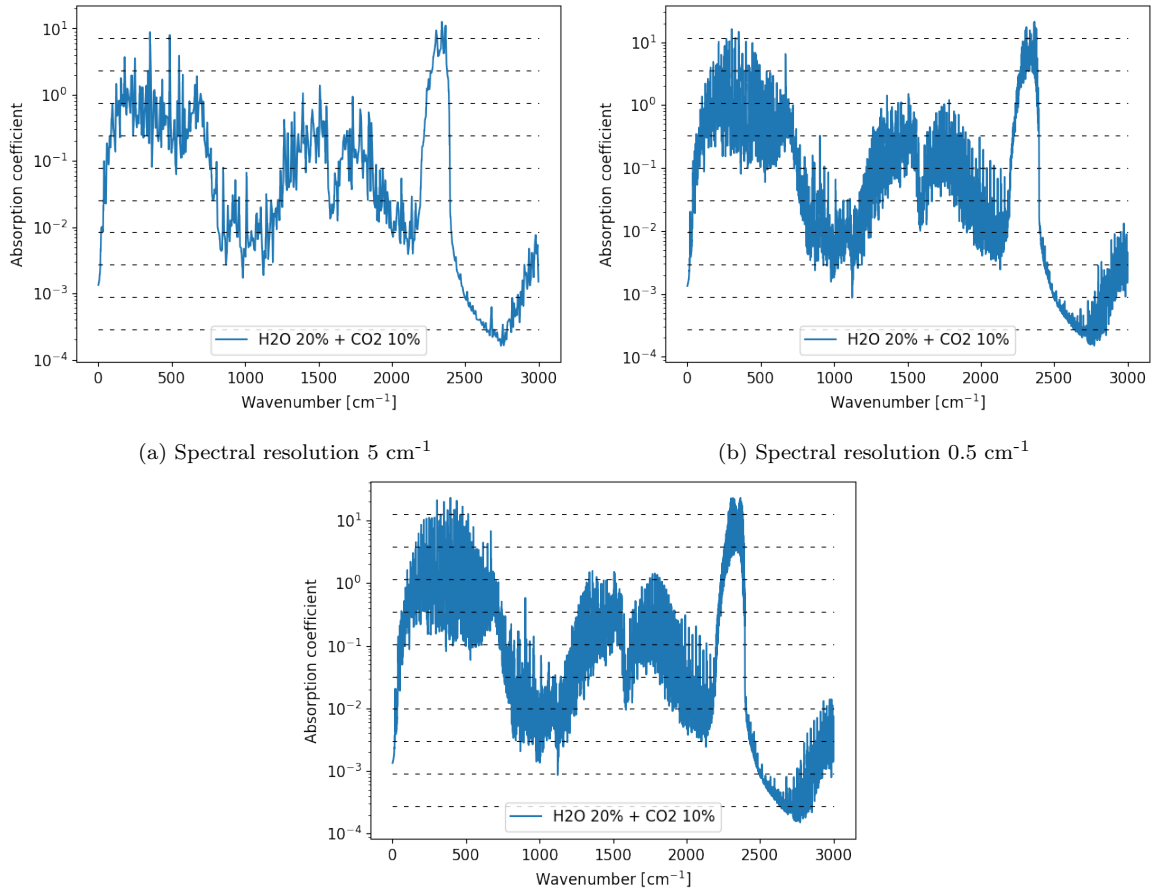

(a) Spectral resolution 5 cm^{-1}

(b) Spectral resolution 0.5 cm^{-1}

(c) Spectral resolution 0.05 cm^{-1}

Figure 3: Absorption coefficient function of the mixture at different spectral resolutions. Dashed lines show an example of discretisation using 10 discrete cross sections.

Figures 6a and 6b show the variation of the relative mean error of the approximations with respect to the benchmark. The variation of the computational cost of solving the RTE with respect to the number of discrete cross sections at each spectral resolution of the absorption cross section profile is shown in figures 6c and 6d.

Finite element expansion performs better in terms of computational cost, this result is consistent with previous studies. However, in terms of accuracy the best result is achieved with spherical harmonics method using the absorption distribution function with the highest spectral resolution and 10 discrete cross sections. In order to investigate the cause of the increased cost for spherical harmonics, we examine the runtime for each discrete cross section.

Figure 7 shows the runtime of calculating the intensity for each discrete cross section (energy group) using spherical harmonics method, for the most accurate case (absorption distribution function with the highest spectral resolution and 10 discrete cross sections) . It can be observed that the runtime is higher for those energy groups with lower Plank absorption coefficient, whilst runtime is significantly lower for those energy groups with higher Plank absorption coefficient. This is due to the unphysical oscillations described in Section 1 in the optically thin groups.

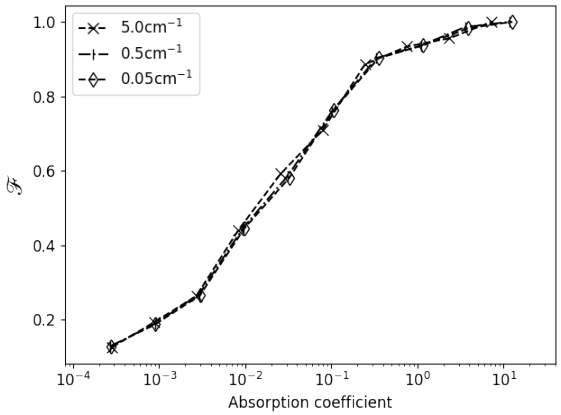

(a) Absorption distribution functions at different spectral resolutions for 10 discrete cross sections.

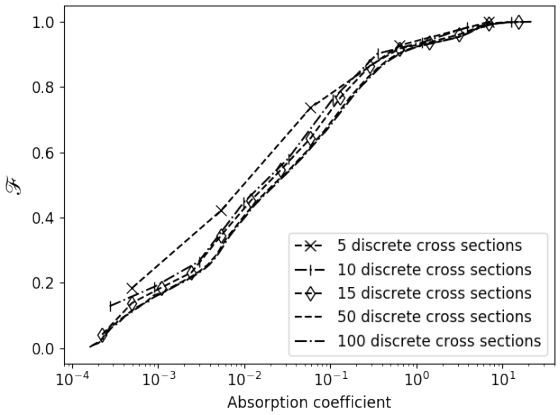

(b) Absorption distribution functions at different numbers of discrete cross sections for 0.05 cm^{-1} resolution.

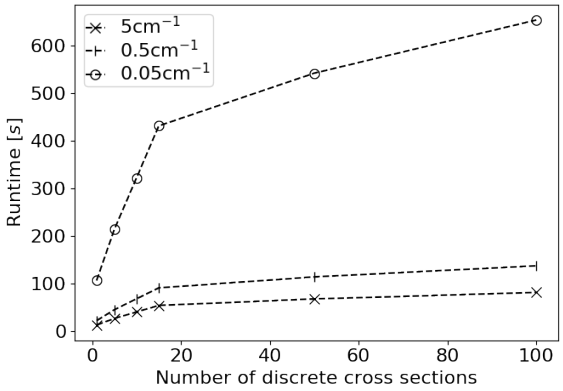

(c) Variation of the computational time of the global gas radiation model as function of the number of discrete cross section for each spectral resolution of the line–by–line absorption cross sections.

Figure 4: (a) Absorption distribution functions at different spectral resolutions, (b) absorption distribution functions for different numbers of discrete cross sections, (c) computational cost of calculating the absorption distribution function.

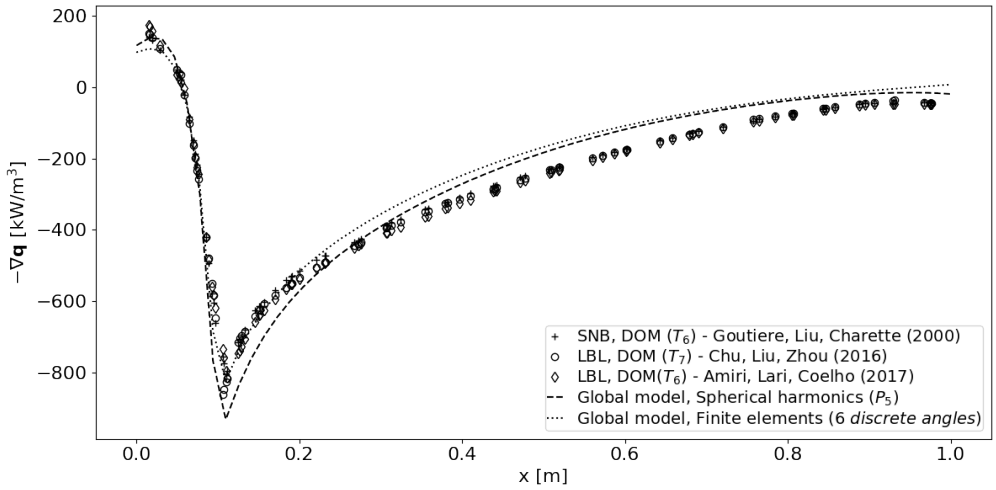

Figure 5: Source term $-\nabla \cdot \mathbf{q}$ along the midline $y = 0.25$.

The oscillations significantly increase the condition number of our linear system when compared to the optically thick groups, which degrades the performance of our iterative method.

Table 1: Summary of benchmark cases.

	Spatial discretisation	Angular discretisation	Gas radiation model
Goutiere, Liu & Charette [13]	Finite volume method (FVM) uniform grid (61×31)	Discrete ordinates method, T_7 quadrature	SNB
Amiri, Lari & Coelho [42]	Finite volume method (FVM) non-uniform grid (31×20)	Discrete ordinates method, T_6 quadrature	LBL
Chu, Liu & Zhou [43]	Finite volume method (FVM) non-uniform grid (21×21)	Discrete ordinates method T_7 quadrature	LBL
Amiri & Lari [44]	Natural element method (NEM) uniform grid (52×27)	Discrete ordinates method, T_6 quadrature	LBL

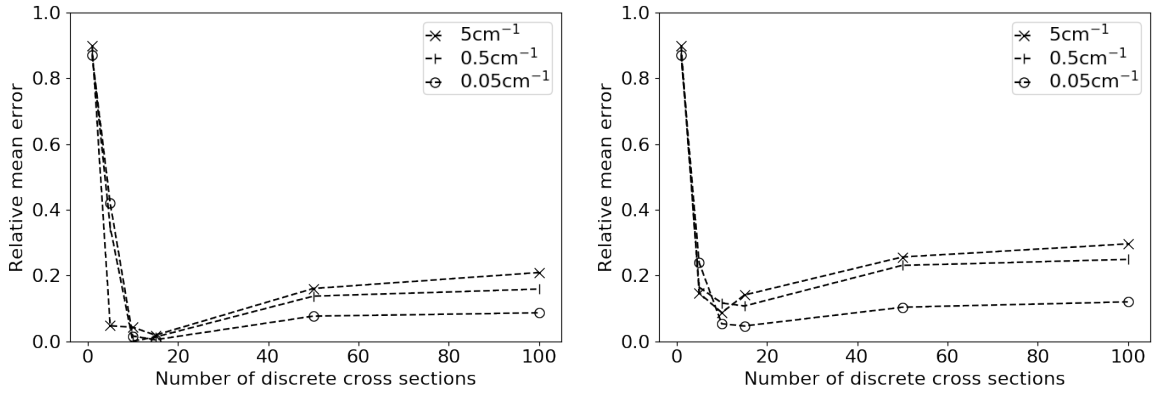

(a) Spherical harmonics.

(b) Finite elements.

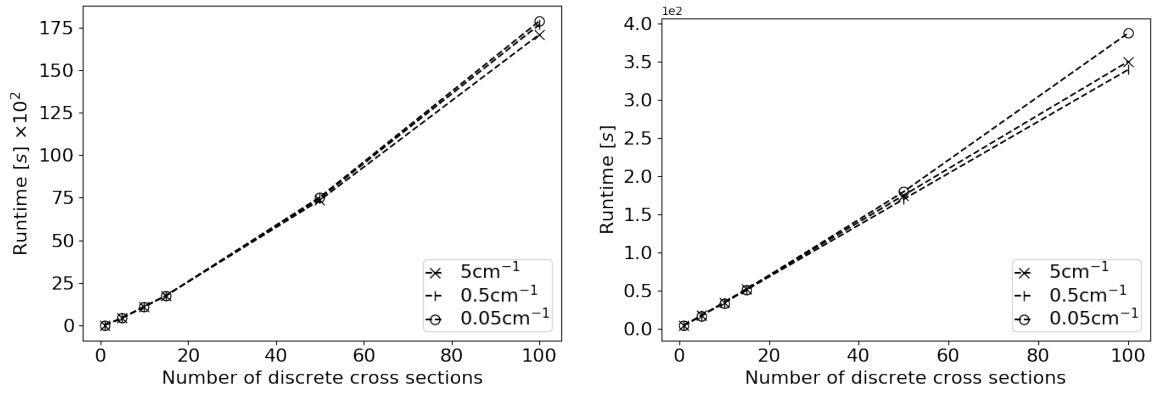

(c) Spherical harmonics.

(d) Finite elements.

Figure 6: Relative mean error of radiative power along the midline $y = 0.25$ using spherical harmonics and finite element expansions as function of the number of discrete cross section for each spectral resolution of absorption cross sections, (a) and (b). Variation of the computational time using spherical harmonics and finite element expansions as function of the number of discrete cross section for each spectral resolution of absorption cross sections, (c) and (d).

In an attempt to tackle this, a new discretisation method for the absorption distribution function is developed to reduce the computational cost of solving the RTE using spherical harmonics method.

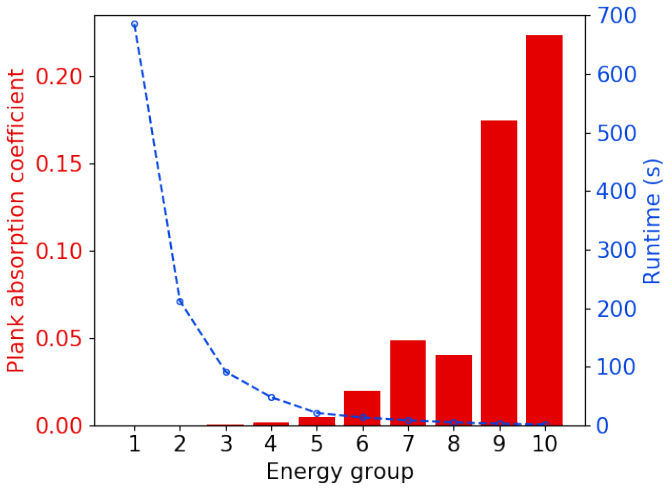

Figure 7: Plank absorption coefficient and computational cost of solving the RTE using spherical harmonics method for each energy group. The absorption distribution function is discretised with a spectral resolution of 0.05cm^{-1} into 10 discrete cross sections (energy groups).

5. Non–uniform discretisation method for the absorption distribution function

Considering that the total intensity is the sum of the contributions of the intensities calculated for each discrete cross section, as shown in Eq. (16), the total computational cost of solving the RTE considers the contributions of solving the RTE for each discrete cross section. In the spherical harmonics method the computational cost is higher for those discrete cross sections in which the Plank absorption coefficient is in the optically thin limit, i.e. $\kappa_{p_i} < \tau_L$ with $\kappa_{p_i} = a_i k_i$ and $\tau_L : \tau \ll 1$. In order to overcome this a new discretisation of the absorption distribution function is introduced, setting the goal as $\kappa_{p_i} > \tau_L$.

The absorption distribution function is a cumulative function, therefore strictly monotonic, where the individual contribution of each discrete cross section to the total intensity can be represented as the area of a bin of a histogram. This histogram corresponds to the non–cumulative distribution $f(C)$ which is the derivative of the cumulative distribution function $\mathscr{F}(C)$. In this histogram the width of the bins is defined by the intervals $[C_i^-, C_i^+]$ where the discrete cross section value C_i lies.

The proposed method consists of an adaptive non–uniform discretisation of a high resolution absorption distribution function, which has been calculated using a high number of discrete cross sections (e.g. 100 discrete cross sections as shown in figure 4b), into a lower number of non uniform intervals $[C_i^{*-}, C_i^{*+}]$ and find $C_i^* \in [C_i^{*-}, C_i^{*+}]$ such that $\tau_L < \kappa_i^* a_i^*$, with $\kappa_i^* = NXC_i^*$ and $a_i^* = \Delta C_i^* f(C_i^*)$. A possible limitation of this method might arise if the whole spectrum is thin or if a very narrow spectrum is considered. In the case of a thin spectrum, it might be difficult to find energy groups that meet the condition $\tau_L < \kappa_i^* a_i^*$ since κ_i values will be small.

In the case of a very narrow spectrum, the feasibility of finding appropriate energy groups will depend on the number of spectral lines data available at the selected spectral range. Figure 8 shows a schematic of this method. Additionally, this method is summarised in algorithm 2. .

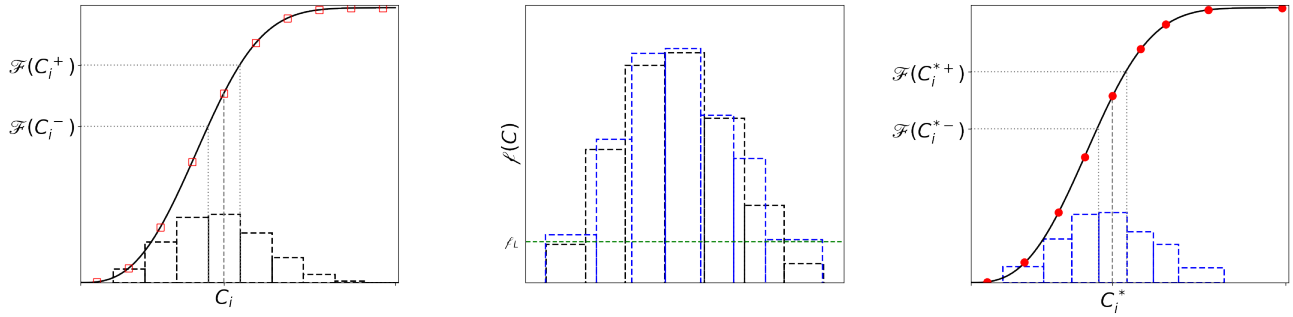

Figure 8: Schematic of the non–uniform method for the absorption distribution function. left: initial absorption distribution function with its corresponding histogram, centre: comparison of the adapted histogram (blue) and the original histogram (black), right: mapping of the discrete cross sections from the adapted histogram into the absorption distribution function for calculation of $a_i^* = \mathscr{F}(C_i^{*-}) - \mathscr{F}(C_i^{*+})$.

Algorithm 2: Adapt non–uniform discrete cross section

Data: High resolution absorption distribution function

Result: Absorption coefficients and weights

Discretise ADF into n intervals;

for i = *1,...,n* **do**

  if $\tau_L < NXC_i a_i$ **then**

    continue;

  else

    Calculate a_i^*;

    Calculate C_i^*;

    Calculate C_i^{+*};

    Update $C_{i+1}^- = C_i^{+*}$;

    Calculate C_{i+1};

  end

  Calculate absorption coefficients weights;

  Calculate absorption coefficients;

end

In order to test this adaptive method, the absorption distribution function at the highest spectral resolution and highest number of cross sections among the cases considered (i.e. 0.05 cm^{-1} and 100 discrete cross sections) was used for calculating different numbers of non–uniform discrete cross sections, between 5 and 50. Figure 9 shows the computational cost of solving the RTE with the new discrete cross section and weight values compared to the reference case (spectral resolution 0.05 cm^{-1} and 100 discrete cross). Additionally, this figure shows the

variation of the relative mean error of the radiative power along the midline $y = 0.25$ calculated the new discrete cross section and weight values with respect to the benchmark presented in [13].

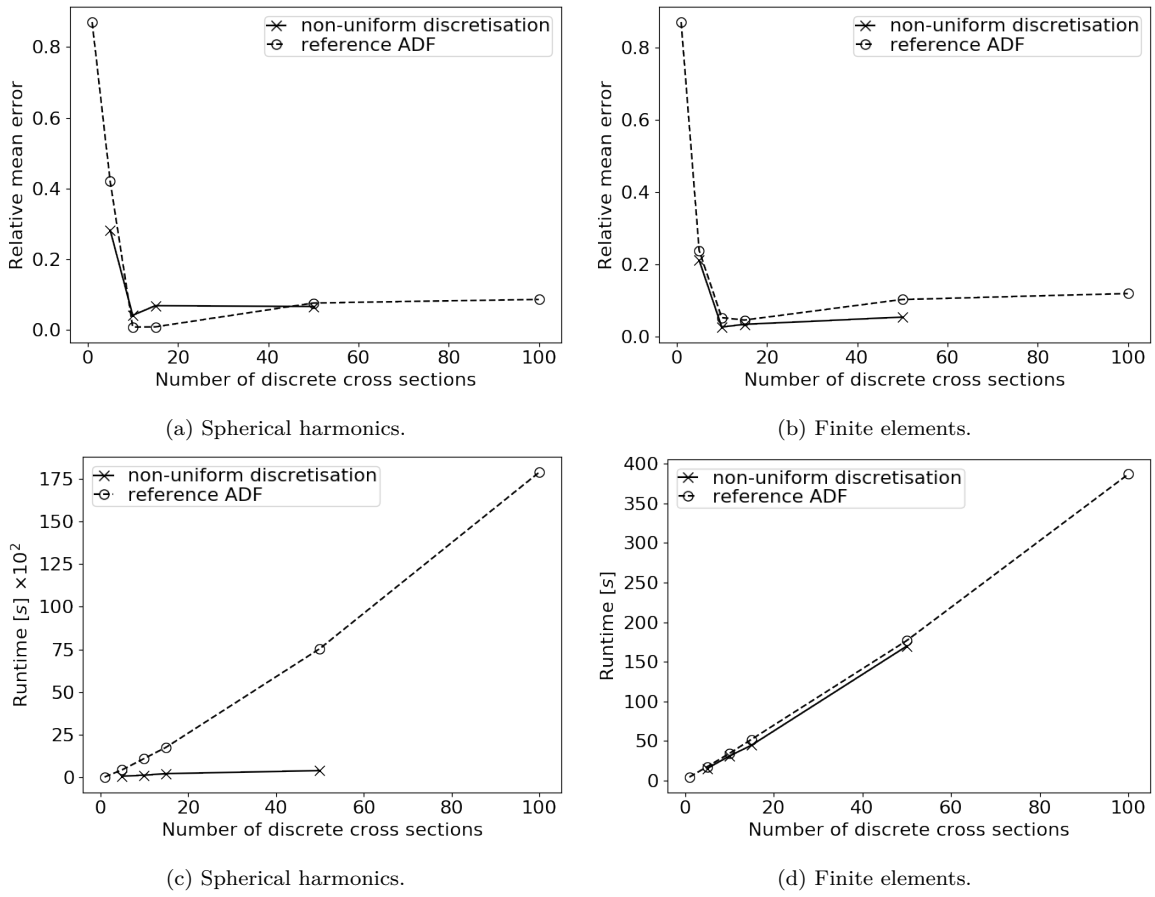

(a) Spherical harmonics.

(b) Finite elements.

(c) Spherical harmonics.

(d) Finite elements.

Figure 9: Comparison of the relative mean error of radiative power along the midline $y = 0.25$ as function of the number of discrete cross sections using spherical harmonics and finite element expansions, (a) and (b). Comparison of the variation of the computational time as function of the number of discrete cross sections, using spherical harmonics and finite element expansions, (c) and (d). The reference ADF has a spectral resolution 0.05 cm^{-1}.

From figures 4c, 9c and 9d it can be concluded that the computational cost of the global gas radiation model is not significant compared to the cost of solving the RTE, therefore, despite the fact that the proposed method implies additional computation of the discrete cross sections, the effect of this additional computation on the total cost is minimal. Furthermore the effect of this non–uniform discretisation of the ADF on the computational cost of solving the RTE using spherical harmonics method is very positive, while ensuring good accuracy. In the case of finite elements in angle, this non–uniform discretisation of the absorption distribution function has a significant effect on the relative error of the radiative power along midline. This significant effect is the result of a mitigation of ray–effects, which manifest when the discrete cross section is low, this is fixed by the non–uniform discretisation of the ADF.

This adaptive method was also tested calculating non–uniform ADFs from the two lower

spectral resolution uniform ADFs (i.e. 5, 0.5 cm^{-1} and 100 discrete cross sections). In those cases, the error values were higher than those shown in figures 9a and 9b with similar computational cost.

A detailed illustration of the effect of the non–uniform discretisation of the absorption distribution function on the computational cost can be observed in figure 10 that shows the runtime of calculating the intensity for each discrete cross section (energy group) using spherical harmonics method as in figure 7. In this case only one energy group remains with a low Plank absorption coefficient value, compared to values of the initial ADF discretisation (figure 7). This leads to a computational cost about one order of magnitude lower for this case.

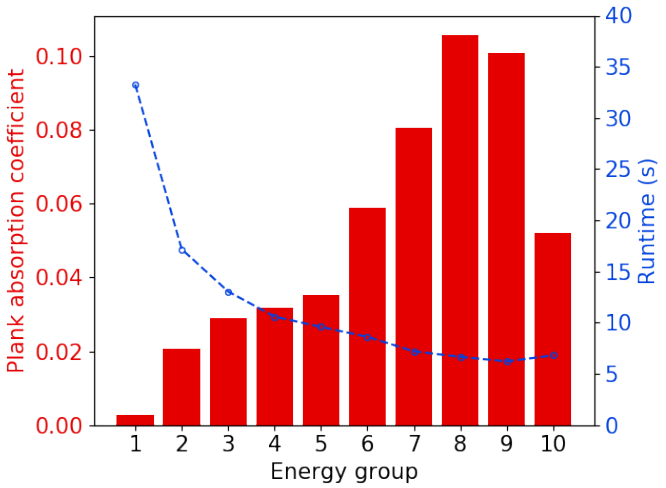

Figure 10: Plank absorption coefficient and computational cost of solving the RTE using spherical harmonics method for each energy group after applying non–uniform discretisation of the absorption distribution function. The absorption distribution function is discretised with a spectral resolution of $0.05 cm^{-1}$ into 10 non–uniform discrete cross sections (energy groups).

Now that we have established that the use of non–uniform discretisation of the ADF has positive effects on both spherical harmonics and finite elements in angle, we turn to using this in a coupled convection–radiation problem with usteady inhomogeneous participating media, which is initially transparent. These conditions are particularly adverse for spherical harmonics, in terms of computational cost, and for finite elements in angle, in terms of ray–effects. Therefore, the non–uniform ADF comes into being suitable and convenient for this problem.

6. Coupled convection–radiation problem

The coupled convection–radiation problem studied corresponds to a rectangular enclosure with differentially–heated black walls as described in figure 11. The parameters for this case

are consistent with the experiments performed by Kim and Viskanta [45]. For brevity, we refer the reader to this study for the experiment details.

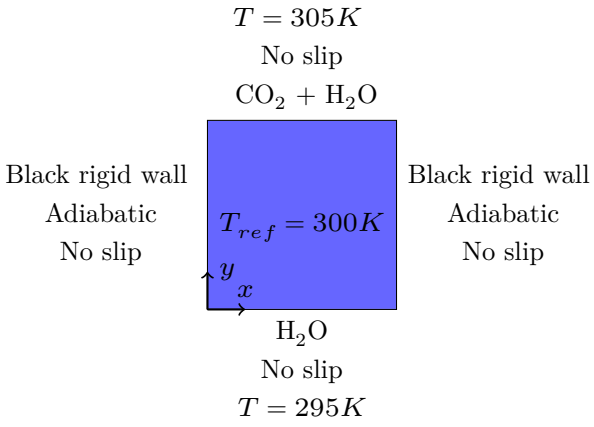

Figure 11: Schematic diagram of the problem.

Three different cases were considered in order to asses the effect of gas radiation and the fluid flow through boundaries and inside the enclosure. The first case does not consider any flow through the boundaries and the only participating medium is considered transparent and homogeneously distributed inside the enclosure. This case is used as a reference to compare the effect of the incoming flows into the rectangular enclosure. The other two cases involve species incoming through the top and bottom boundaries, which makes the participating media both inhomogeneous and unsteady. The flows are described by the boundary conditions $-(\overline{\overline{D}}\nabla C)\cdot\hat{\mathbf{n}} = h(C - C_\infty)$. One of the cases considers the participating media as grey gases and the other one considers the participating media as non–grey gases. The cases are summarised in table 2.

Table 2: Summary of test cases.

Case	Top wall condition	Bottom wall condition	Gas radiation approach
1	$-(\overline{\overline{D}}\nabla C)\cdot\hat{\mathbf{n}} = 0$	$-(\overline{\overline{D}}\nabla C)\cdot\hat{\mathbf{n}} = 0$	–
2	$-(\overline{\overline{D}}\nabla C)\cdot\hat{\mathbf{n}} = h(C - C_\infty)$	$-(\overline{\overline{D}}\nabla C)\cdot\hat{\mathbf{n}} = h(C - C_\infty)$	Grey gas
3	$-(\overline{\overline{D}}\nabla C)\cdot\hat{\mathbf{n}} = h(C - C_\infty)$	$-(\overline{\overline{D}}\nabla C)\cdot\hat{\mathbf{n}} = h(C - C_\infty)$	Non–grey gas

The problem presented in figure 11 was solved numerically over an unstructured mesh with 4426 elements using a $\mathrm{P_{1DG}} - \mathrm{P_2}$ discretisation element pair for velocity and pressure, and control volume finite element discretisation for the temperature and for the species incoming through the boundaries. For time integration a Crank–Nicolson scheme was used ($\Theta = 0.5$).

The properties of the participating media are modelled using absorption distribution functions for each of the incoming fluids, applying the mixture approach for the species incoming

through the top boundary. The absorption coefficients are calculated from 10 discrete cross sections defined using the method shown in algorithm 2.

The absorption cross sections were calculated from HITRAN2016 data at the spectral range 0–3000 cm^{-1} with a resolution of 0.05 cm^{-1}.

6.1. Results

The RTE was solved using both spherical harmonics (P_3) and finite elements in angle (6 discrete angles) with explicit coupling between flow and radiation solvers, updating the radiative source term at every convection time step. The formulation of the boundary conditions introduces an inhomogeneous unsteady participating media.

For the non–grey gases case, both the uniform and non-uniform discretisations of the absorption distribution function were used in order to compare the effect of the non–uniform discretisation method when using the spherical harmonics method for this problem. Comparing the non–uniform discretisation method to the initial discretisation of the ADF, there is a pointwise maximum relative difference of the radiative power field across the domain below 4%. This confirms the non-uniform ADF does not significantly increase the error in this problem.

The runtime of solving the RTE using spherical harmonics and the initial discretisation of the ADF was 1.43×10^5 s, whilst the runtime of solving the RTE using spherical harmonics and the non–uniform discretisation method of the ADF was 3.78×10^4 s. This runtime is closer to that of solving the RTE using finite elements in angle (1.2×10^4 s). Like in Section 5, the non-uniform ADF increases the performance of spherical harmonics significantly. Examining this further, for the spherical harmonics method the runtime per time step depends on the optical thickness of the participating media. Figure 12 shows the runtime per time step for solving the RTE using spherical harmonics and the initial discretisation of the ADF, using spherical harmonics and the non–uniform discretisation method of the ADF and using finite elements in angle. The non–uniform discretisation of the ADF significantly decreases the runtime during early time steps. Finite elements in angle are not sensitive to optical thickness in terms of computational cost.

Although the finite elements runtime is not sensitive to optical thickness, of course the error in the simulation at early time is sensitive to optical thickness, as the participating media is initially transparent, and hence we know that ray–effects will be present at early time in the finite elements in angle solution. Figure 13a shows the ray–effects for finite elements in angle and figure 13b shows the ray–effect free solution for the spherical harmonics method, which is rotationally invariant.

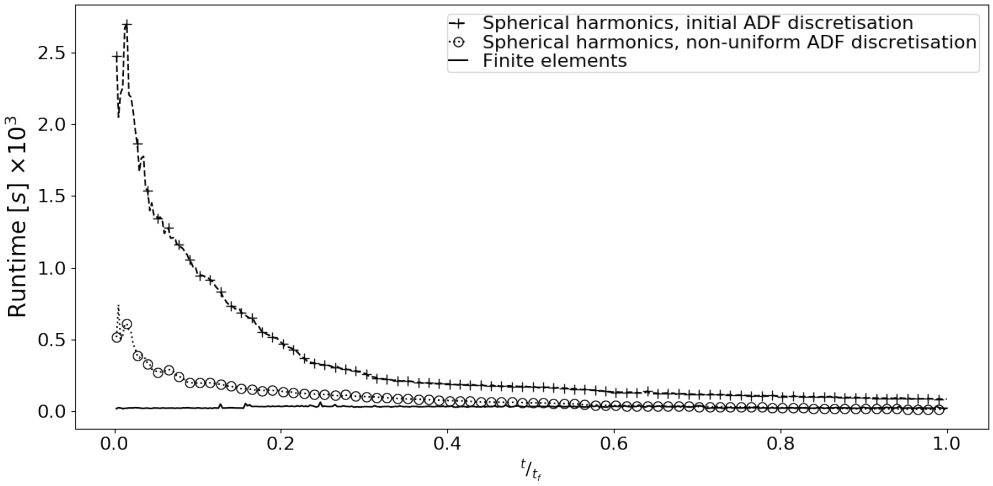

Figure 12: Runtime per time step for non–grey gas case. Dimensionless time is shown in abscissa, i.e $t/t_f = 0$ is the initial condition and $t/t_f = 1$ is the end of the simulation.

The non–uniform discretisation method thus enables the spherical harmonics method as a ray–effect free alternative which is competitive in terms of computational cost. Based on this, only the results with the non–uniform discretisation method of the absorption distribution function are used for further analysis in this study.

(a) Finite elements in angle

(b) Spherical harmonics method

Figure 13: Scalar particle flux across the domain at dimensionless time $t/t_f = 0.00625$. Ray–effects can be observed in the solution calculated using finite elements in angle (six discrete angles), whilst the solution calculated using the spherical harmonics method is free of ray–effects.

Figure 14 shows the incoming flows of species through the top and bottom boundaries at three different time levels. These species are advected by the velocity field generated by natural convection. Points K, L and M are referenced for further analysis of the effect of the unsteady inhomogeneous media on the the temperature field.

Natural convection occurrence depends on fluid properties and temperature field. In this problem species incoming through the boundaries do not affect the fluid properties and are

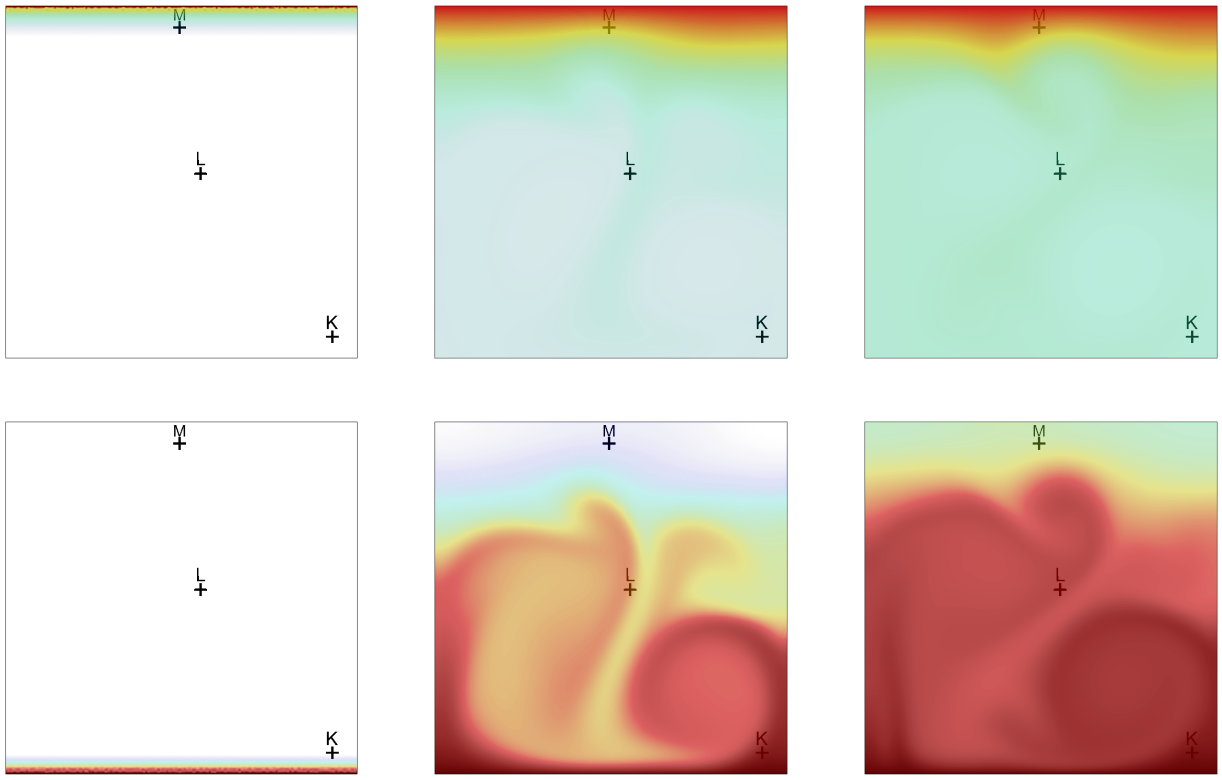

Figure 14: Incoming flow through the boundaries at different time levels. Left: dimensionless time $t/t_f = 0.00625$. Centre: dimensionless time $t/t_f = 0.3$. Right: dimensionless time $t/t_f = 0.45$. Top: flow through top boundary. Bottom: flow through bottom boundary.

considered to be advected by the bulk velocity of the medium. However, gas radiation affects the temperature field inside the enclosure due to the explicit coupling between the fluids and radiation solvers.

Points K, L and M have been defined to track the effect of gas radiation considering the inhomogeneity of the participating media as observed in figure 14. At point K the participating media is mostly composed of H_2O which is entering the enclosure through the bottom boundary. In similar fashion at point M, the participating media is mostly composed of the mixture of CO_2 and H_2O which is entering the enclosure through the top boundary. In contrast, at point L both gases are actively participating.

In order to identify the effect of gas radiation on the temperature field, the difference in temperature in cases 2 and 3 with respect to case 1 has been calculated at all time levels. Figure 15 shows this difference in temperature at points K, L and M.

The temperature difference between the cases that involve gas radiation and case 1 is variable until the enclosure is saturated by the species entering through the boundaries. When that saturation state is achieved, the participating media becomes steady. However, the participating media remains inhomogeneous, thus the temperature difference at points K, L and M have

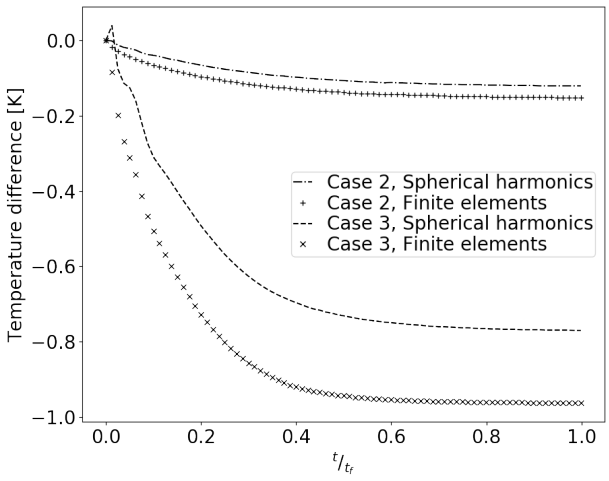

(a) Point K

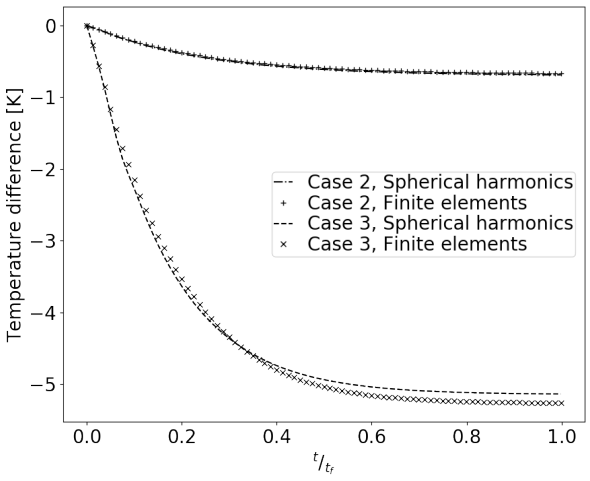

(b) Point L

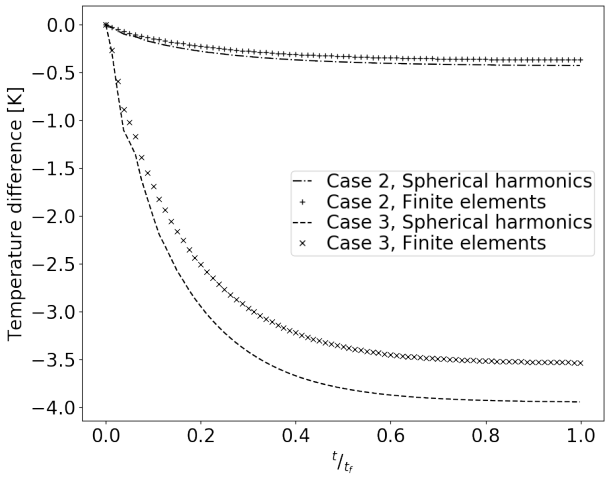

(c) Point M

Figure 15: Difference in temperature for case 1 at points K, L and M during the simulation time.

different values at that steady state.

In cases 2 and 3 there is a physical effect of gas radiation on the temperature field. This effect is highly dependant on the gas radiation approach and the material properties of the species.

In relation to the gas radiation approach, under the grey gas approach (case 2) this effect is considerably lower than under the non–grey gas approach (case 3). The grey gas approach leads to an underestimation of the radiative source term, and consequently an underestimation of the effect of gas radiation on the temperature field. This demonstrates the disadvantage of using the grey gas approach, which is used in engineering problems due to its simplicity and low computational cost. Thus, the non–uniform ADF model introduced in this work arises as

a better alternative that gives significantly improved results without a substantial increase in the computational cost.

The effect of the radiative properties of the species on the temperature field can be observed by comparing the temperature difference at different regions of the enclosure using points K, L and M as reference. In a region of the enclosure in which the participating media is mainly H_2O, the temperature difference is lower since H_2O has a lower absorption cross section. This can be observed in temperature difference values in figure 15a. Likewise, in regions in which the participating media includes a mixture containing CO_2 the temperature difference is higher. This is an expected result considering that the absorption distribution cross section of CO_2 is higher than the absorption distribution cross section of H_2O. Additionally, the results are consistent for the inhomogeneous participating media during the simulated time including both unsteady and steady states. This shows the suitability of the global gas radiation model for inhomogeneous unsteady participating media and its capability to represent effectively the material properties of the species considered as participating media.

Considering the characteristics of the participating media, results calculated using finite elements in angle differ from those calculated using spherical harmonics. These differences are higher in regions where the participating media is thinner due to the aforementioned causes of error such as ray–effects and unphysical oscillations. These differences should reduce as the angular resolution is increased, i.e., through the use of higher numbers of discrete angles in the finite elements case and higher order expansions in the spherical harmonics case. However, this increases the computational cost of the solutions considerably.

7. Conclusions & future work

In this work coupled convection–radiation with an inhomogeneous unsteady participating media has been studied numerically using spherical harmonics and finite elements for the angular discretisation of the radiative transfer equation. To identify the effects of the inhomogeneous unsteady participating media the resulting temperature field was analysed. Results showed that an inhomogeneous participating media has a significant effect on the temperature field. This effect is consistent during unsteady and steady state conditions and depends on the absorption cross section of the species. Additionally, the absorption cross section of species and mixtures of species can be effectively represented by appropriate absorption distribution functions, and thus a global gas radiation model is suitable for coupled convection–radiation problems involving inhomogeneous unsteady participating media with emitting, absorbing, non-scattering media surrounded by grey walls. This approach can be

extended to other applications, however further work is required, e.g. to determine the effect of the choice of reference temperature, used for calculating of the absorption cross section, in applications with high temperature gradient inside the domain.

A new method for gas radiation based on an absorption distribution function has been introduced. This method involves a non–uniform discretisation of the spectrum and the calculation of appropriate absorption coefficients and weight values that lead to a considerable reduction in the computational cost of the spherical harmonics method without significantly affecting accuracy. This makes the spherical harmonics method a competitive option in terms of computational cost for cases where ray–effects are undesirable. Additionally, the non–uniform discretisation of the ADF has a positive effect on finite elements in angle by mitigating ray–effects, and this mitigation leads to an improvement of accuracy without affecting computational cost.

This work helps to show that trying to quantify the differences between angular discretisation methods is difficult without first examining individual benchmarks and hence the absorption distribution function and cross-sections. These factors are crucial not only for the accuracy but also for the runtime performance of each angular discretisation method and can obscure the advantages or disadvantages of each within coupled radiative transfer problems.

A future focus for this work would be to examine the role of the non–uniform absorption distribution function on other angular discretisations and analyse the limits on performance for non-uniform absorption distribution function.

8. Acknowledgements

This work was funded under the scholarship programme No. 783 of the Ministry of science, technology and innovation of Colombia and sponsorship from Grupo Nutresa S.A.

References

[1] Aydin O, Yang WJ. Natural convection in enclosures with localized heating from below and symmetrical cooling from sides. International Journal of Numerical Methods for Heat and Fluid Flow. 2000;10(5):518–529.

[2] Wang Y, Meng X, Yang X, Liu J. Influence of convection and radiation on the thermal environment in an industrial building with buoyancy-driven natural ventilation. Energy and Buildings. 2014;75:394 – 401.

[3] Coelho PJ. Numerical simulation of the interaction between turbulence and radiation in reactive

flows. Progress in Energy and Combustion Science. 2007;33(4):311–383. Available from: https://www.sciencedirect.com/science/article/pii/S036012850600061X.

[4] Dombrovsky LA. Scattering of Radiation and Simple Approaches to Radiative Transfer in Thermal Engineering and Biomedical Applications. In: Springer series in light scattering. Springer; 2019. p. 71–127.

[5] Sun Y, Zhang X, Howell JR. Assessment of different radiative transfer equation solvers for combined natural convection and radiation heat transfer problems. Journal of Quantitative Spectroscopy and Radiative Transfer. 2017;194:31 – 46.

[6] Miroshnichenko IV, Sheremet MA. Turbulent natural convection heat transfer in rectangular enclosures using experimental and numerical approaches: A review. Renewable and Sustainable Energy Reviews. 2018;82:40 – 59.

[7] Tian YS, Karayiannis TG. Low turbulence natural convection in an air filled square cavity: Part I: the thermal and fluid flow fields. International Journal of Heat and Mass Transfer. 2000;43(6):849 – 866.

[8] Ampofo F, Karayiannis TG. Experimental benchmark data for turbulent natural convection in an air filled square cavity. International Journal of Heat and Mass Transfer. 2003;46(19):3551 – 3572.

[9] Soucasse L, Rivière P, Soufiani A, Xin S, Le Quéré P. Transitional regimes of natural convection in a differentially heated cubical cavity under the effects of wall and molecular gas radiation. Physics of Fluids. 2014;26(2).

[10] Modest MF. Radiative Heat Transfer. 3rd ed. Academic press; 2013.

[11] Kez V, Liu F, Consalvi JL, Ströhle J, Epple B. A comprehensive evaluation of different radiation models in a gas turbine combustor under conditions of oxy-fuel combustion with dry recycle. Journal of Quantitative Spectroscopy and Radiative Transfer. 2016;172:121 – 133.

[12] Solovjov VP, Webb BW, Andre F. Radiative properties of gases. Handbook of thermal science and engineering. 2017;2:1069e1142.

[13] Goutiere V, Liu F, Charette A. An assessment of real-gas modelling in 2D enclosures. Journal of Quantitative Spectroscopy and Radiative Transfer. 2000;64(3):299 – 326.

[14] Solovjov VP, Webb BW. Global Spectral Methods in Gas Radiation: The Exact Limit of the SLW Model and Its Relationship to the ADF and FSK Methods. Journal of Heat Transfer. 2011 01;133(4).

[15] Pierrot L, Soufiani A, Taine J. Accuracy of narrow-band and global models for radiative transfer in H2O, CO2, and H2O CO2 mixtures at high temperature. Journal of Quantitative Spectroscopy and Radiative Transfer. 1999;62(5):523 – 548.

[16] Chu H, Liu F, Zhou H. Calculations of gas thermal radiation transfer in one-dimensional planar enclosure using LBL and SNB models. International Journal of Heat and Mass Transfer. 2011;54(21):4736 – 4745.

[17] Zeng X, Liang C, Duan L, Chen X, Liu D, Ma J. A GPU-based line-by-line method for thermal radiation transfer of H2O, CO2, and H2O/CO2 mixture. Applied Thermal Engineering. 2020;167:114799.

[18] Chu H, Gu M, Consalvi JL, Liu F, Zhou H. Effects of total pressure on non-grey gas radiation transfer in oxy-fuel combustion using the LBL, SNB, SNBCK, WSGG, and FSCK methods. Journal of Quantitative Spectroscopy and Radiative Transfer. 2016;172:24 – 35.

[19] Solovjov VP, Webb BW. SLW modeling of radiative transfer in multicomponent gas mixtures. Journal of Quantitative Spectroscopy and Radiative Transfer. 2000;65(4):655 – 672.

[20] Malalasekera W. Numerical calculation of radiative heat transfer. In: An introduction to computational fluid dynamics: the finite volume method. PEARSON Prentice Hall; 2007. .

[21] Soucasse L, Rivière P, Soufiani A. Natural convection in a differentially heated cubical cavity under the effects of wall and molecular gas radiation at Rayleigh numbers up to 3×10^9. International Journal of Heat and Fluid Flow. 2016;61:510 – 530.

[22] Buchan AG, Pain CC, Eaton MD, Smedley-Stevenson RP, Goddard AJH. Linear and quadratic octahedral wavelets on the sphere for angular discretisations of the Boltzmann transport equation. Annals of Nuclear Energy. 2005;32(11):1224 – 1273.

[23] Sun Y, Zhang X, Howell JR. Evaluation of three different radiative transfer equation solvers for combined conduction and radiation heat transfer. Journal of Quantitative Spectroscopy and Radiative Transfer. 2016;184:262 – 273.

[24] Coelho PJ. Advances in the discrete ordinates and finite volume methods for the solution of radiative heat transfer problems in participating media. Journal of Quantitative Spectroscopy and Radiative Transfer. 2014;145:121 – 146.

[25] Soucasse L, Dargaville S, Buchan AG, Pain CC. A goal-based angular adaptivity method for thermal radiation modelling in non grey media. Journal of Quantitative Spectroscopy and Radiative Transfer. 2017;200:215–224.

[26] St Aubin J, Keyvanloo A, Fallone BG. Discontinuous finite element space-angle treatment of the first order linear Boltzmann transport equation with magnetic fields: Application to MRI-guided radiotherapy. Medical Physics. 2016;43(1):195–204.

[27] Soucasse L, Buchan AG, Dargaville S, Pain CC. An angular reduced order model for radiative transfer in non grey media. Journal of Quantitative Spectroscopy and Radiative Transfer. 2019;229:23 – 32.

[28] Merton SR, Pain CC, Smedley-Stevenson RP, Buchan AG, Eaton MD. Optimal discontinuous finite element methods for the Boltzmann transport equation with arbitrary discretisation in angle. Annals of Nuclear Energy. 2008;35(9):1741 – 1759.

[29] Morel JE, Wareing TA, Lowrie RB, Parsons DK. Analysis of Ray-Effect Mitigation Techniques. Nuclear Science and Engineering. 2003;144(1):1–22.

[30] Koch R, Krebs W, Wittig S, Viskanta R. Discrete ordinates quadrature schemes for multidimensional radiative transfer. Journal of Quantitative Spectroscopy and Radiative Transfer. 1995;53(4):353 – 372.

[31] Hughes TJR, Feijóo GR, Mazzei L, Quincy JB. The variational multiscale method—a paradigm for computational mechanics. Computer Methods in Applied Mechanics and Engineering. 1998;166(1):3 – 24.

[32] Hughes TJR, Scovazzi G, Bochev PB, Buffa A. A multiscale discontinuous Galerkin method with the computational structure of a continuous Galerkin method. Computer Methods in Applied Mechanics and Engineering. 2006;195(19):2761 – 2787.

[33] Candy AS. Subgrid scale modelling of transport processes [Ph.D. thesis]. Imperial College London; 2008.

[34] Buchan AG, Candy AS, Merton SR, Pain CC, Hadi JI, Eaton MD, et al. The inner-element subgrid scale finite element method for the Boltzmann transport equation. Nuclear Science and Engineering. 2010;164(2):105–121.

[35] Gordon IE, Rothman LS, Hill C, Kochanov RV, Tan Y, Bernath PF, et al. The HITRAN2016 molecular spectroscopic database. Journal of Quantitative Spectroscopy and Radiative Transfer. 2017;203:3 – 69. HITRAN2016 Special Issue.

[36] Laraia AL, Gamache RR, Lamouroux J, Gordon IE, Rothman LS. Total internal partition sums to support planetary remote sensing. Icarus. 2011;215(1):391 – 400.

[37] Pain CC, de Oliveira CRE, Goddard AJH, Umpleby AP. Non-linear space-dependent kinetics for the criticality assessment of fissile solutions. Progress in Nuclear Energy. 2001;39(1):53 – 114.

[38] Goffin MA, Buchan AG, Dargaville S, Pain CC, Smith PN, Smedley-Stevenson RP. Goal-based angular adaptivity applied to a wavelet-based discretisation of the neutral particle transport equation. Journal of Computational Physics. 2015;281:1032–1062.

[39] Dargaville S, Goffin MA, Buchan AG, Pain CC, Smedley-Stevenson RP, Smith PN, et al. Solving the Boltzmann transport equation with multigrid and adaptive space/angle discretisations. Annals of Nuclear Energy. 2015;86:99 – 107.

[40] Piggott MD, Gorman GJ, Pain CC, Allison PA, Candy AS, Martin BT, et al. A new computational framework for multi-scale ocean modelling based on adapting unstructured meshes. Int J Numer Methods Fluids. 2008;56(8):1003–1015.

[41] AMCG ICL. Fluidity manual v4.1.12. figshare; 2015. Available from: https://figshare.com/articles/journal_contribution/Fluidity_Manual/1387713/2.

[42] Amiri H, Lari K, Coelho PJ. Comparison of CK model and line by line method using old and updated parameters/databases. International Journal of Thermal Sciences. 2017;118:448 – 460.

[43] Chu H, Liu F, Zhou H. Calculations of gas radiation heat transfer in a two-dimensional rectangular enclosure using the line-by-line approach and the statistical narrow-band correlated-k model. International Journal of Thermal Sciences. 2012;59:66 – 74.

[44] Amiri H, Lari K. Line by line benchmark solutions for radiative heat transfer in 2D irregular enclosures with non-gray media. International Journal of Thermal Sciences. 2018;133:307 – 319.

[45] Kim D, Viskanta R. Study of the effects of wall conductance on natural convection in differently oriented square cavities. Journal of Fluid Mechanics. 1984;144:153–176.